Oxygen-alloyed poly-Si passivating contacts for high-thermal budget c-Si heterojunction solar cells

Yang, Guangtao; Han, Can; Procel, Paul; Zhao, Yifeng; Singh, Manvika; Mazzarella, Luana; Zeman, Miro; Isabella, Olindo

DOI
10.1002/pip.3472

Publication date
2022

Document Version
Final published version

Published in
Progress in Photovoltaics: research and applications

Received: 5 May 2021 | Revised: 5 August 2021 | Accepted: 1 September 2021

DOI: 10.1002/pip.3472

RESEARCH ARTICLE

PROGRESS IN PHOTOVOLTAICS WILEY

Oxygen-alloyed poly-Si passivating contacts for high-thermal budget c-Si heterojunction solar cells

Guangtao Yang | Can Han | Paul Procel | Yifeng Zhao | Manvika Singh | Luana Mazzarella | Miro Zeman | Olindo Isabella

Photovoltaic Materials and Devices group, Delft University of Technology, Delft, The Netherlands

Correspondence
G. Yang and O. Isabella, Photovoltaic Materials and Devices Group, Electrical Sustainable Energy Department, Delft University of Technology, Mekelweg 4, Delft 2628 CD, The Netherlands.
Email: g.yang@tudelft.nl; o.isabella@tudelft.nl

Funding information
Topsector Energie of the Dutch Ministry of Economic Affairs, Grant/Award Numbers: TEUE117010, TEUE118002

Abstract

Crystalline silicon solar cells with passivating contacts based on doped poly-Si exhibit high optical parasitic losses. Aiming at minimizing these losses, we developed the oxygen-alloyed poly-Si (poly-SiO_x) as suitable material for passivating contacts. From passivation point of view, poly-SiO_x layers show excellent passivation quality and carrier selectivity for both *n*-type ($iV_{OC,flat} = 740$ mV, contact resistance $\rho_c = 0.7$ mΩ/cm^2, $iV_{OC,textured} = 723$ mV) and *p*-type ($iV_{OC,flat} = 709$ mV, $\rho_c = 0.5$ mΩ/cm^2). Optically, due to the incorporation of oxygen, the absorption coefficient of poly-SiO_x becomes much lower than that of doped poly-Si at long wavelength. Both *n*-type and *p*-type poly-SiO_x layers are concurrently deployed in front/back-contacted (FBC) solar cells with a front indium tin oxide (ITO) layer to facilitate the lateral transport of carriers and minimize cell's reflection. A high cell *FF* of 83.5% obtained in double-side flat FBC solar cell indicates an efficient carrier collection by these passivating contacts. An active-area cell efficiency of 21.0% featuring $J_{SC,EQE} = 39.7$ mA/cm^2 is obtained in front-side textured poly-SiO_x FBC cell, with the potential of further improvement in both V_{OC} and *FF*. The optical advantage of poly-SiO_x over poly-Si as passivating contact is also observed with a 19.7% interdigitated back-contacted (IBC) solar cell endowed with poly-SiO_x emitter and back surface field. Compared to the reference 23.0% IBC solar cell with poly-Si passivating contacts, the one based on poly-SiO_x passivating contacts shows higher IQE at wavelengths above 1100 nm. This indicates that for both FBC and IBC cells, poly-SiO_x passivating contacts hold potential in enhancing the cell J_{SC} by maximizing the cell spectral response.

KEYWORDS
c-Si solar cells, high passivation quality, low absorption coefficient, oxygen-alloyed poly-Si

1 | INTRODUCTION

Great progresses in improving the performance of c-Si solar cells have been achieved by photovoltaic (PV) research institutes[1–17] and industries[18–23] by using poly-Si-based carrier-selective passivating contacts, which feature excellent passivation quality and carrier selectivity. With such passivating contacts, record efficiencies were obtained with both front/back-contacted (FBC) and interdigitated

back-contacted (IBC) solar cell architectures.[1,24] Even though in most FBC cases the poly-Si passivating contact layers are placed at the back side of the cell structures,[3–5,7,10,18–23] solar cells with a poly-Si passivating contact layer at the front side are also under investigation.[25–28] Their potential performance is not as high as compared to those with the poly-Si passivating contact(s) only deployed at the cell back side. This is mainly due to the high absorption of highly doped poly-Si materials, especially when placed at the illuminated side of solar cells.[25] Studies show that when using the poly-Si passivating contact layer at the front side of the cell, about 0.4–1 mA/cm^2 is lost in J_{SC} for every 10 nm of poly-Si material depending on the layer properties and solar cell structures.[29–31] Three main approaches are proposed within the PV community to minimize this optical loss. The first is by simply thinning the poly-Si layer thickness. This approach could solve this optical problem only partially due to the high absorption coefficient of the poly-Si layer. Further, it leads to more challenges on the solar cell electrical performances such as the selection of transparent conductive oxide (TCO) layers and the deployment of specific metallization steps, for example, the firing through process. The second approach is by modifying the solar cell structure, for example, by etching away the poly-Si materials between the metal fingers, which is also called as poly-finger[32] or Passivated Rear and Front ConTacts (PeRFeCT) structure.[33] This approach optically solves the poly-Si absorption issue without influencing the poly-Si metallization processes. However, the complexity of such solar cell demands additional processing steps, including the alignment between the poly-Si fingers and the metal fingers, which are not preferred in the mass production. The third approach is by using more transparent passivating contact materials. The main reasons for the high absorption of the poly-Si passivating contact materials are (i) the low bandgap (similar to c-Si) and (ii) the large free carrier absorption (FCA) due to the heavy doping within the materials.[29,30] However, the high doping level of poly-Si is one of the key factors for achieving high field-effect passivation, limiting the solutions for lowering the FCA. On the compositional side, passivating contact materials minimizing this absorption loss can also be achieved by widening the optical bandgap by alloying the poly-Si with carbon or oxygen.[34–36] Studies on the poly-SiC$_x$ alloys as passivating contacts demonstrate excellent passivation and low contact resistivity,[2,34,37] while a lower absorption in the short wavelength range is observed.[38] Alloying oxygen into poly-Si material, forming poly-SiO$_x$, changes the polycrystalline structure of poly-Si into a mixed phase structure, which makes it another candidate for low absorptive, high passivation capability passivating contact.[7,36,38–41] Therefore, research and development of such materials for solar cell application is attractive for PV community. In fact, a detailed scientific study, in which passivation properties of the poly-SiO$_x$ passivating contacts are related to process parameters, is required to successfully implement this new material in the solar cell process flow.

In this contribution, we elaborate on the application of wide-bandgap poly-SiO$_x$-based passivating contact in high-efficiency FBC and IBC solar cells. The poly-SiO$_x$ was fabricated by crystallizing at high temperature the in situ doped a-SiO$_x$:H layers realized with plasma-enhanced chemical vapor deposition (PECVD). First, we aim at understanding the relation between the PECVD parameters for depositing a-SiO$_x$:H and the structural, optical, and passivation properties of the obtained poly-SiO$_x$ materials. Then, we study the relation between the annealing thermal budget and the passivation properties of poly-SiO$_x$ passivating contacts. The carrier transport properties of our doped poly-SiO$_x$ layers are further investigated in double-side flat FBC solar cells. By means of our newly developed liftoff patterning process, we also implement doped poly-SiO$_x$ passivating contacts in IBC solar cells. Finally, we address the optical enhancement obtained using poly-SiO$_x$ passivating contacts with respect to standard poly-Si counterparts applied in both FBC and IBC solar cells.

2 | EXPERIMENTAL DETAILS

The c-Si bulk material used in this work is n-type double-side polished (DSP) FZ c-Si wafers (orientation: <100>, resistivity: 1–5 Ω cm). The thickness of the wafers before texturing with trimethylammonium hydroxide (TMAH) is 280 ± 20 μm. For sample preparation, the c-Si wafer is first cleaned in HNO_3 (99%) to remove eventual organic contaminations and then in HNO_3 (68%, at 110°C) to remove inorganic contaminations. A dip in 0.55% HF is used to remove the SiO_2 layer grown during such cleaning steps. The ultrathin tunneling SiO$_x$ is prepared with nitric acid oxidation of silicon (NAOS) approach, which results a ∼1.4-nm-thick NAOS–SiO$_x$.[42] To prepare poly-SiO$_x$ passivating contacts, the PECVD a-SiO$_x$:H layers deposited on top of the NAOS–SiO$_x$ contain two separate sub-layers, a 10-nm-thick intrinsic a-SiO$_x$:H layer capped with a doped a-SiO$_x$:H layer with variable thickness and doping level. This bilayer configuration is needed because the intrinsic layer acts as a buffer layer for the diffusion of dopants from the doped layer, leading to a higher passivation quality.[39,43–45] The temperature is 180°C during the PECVD; CO_2 is used as O source, and PH_3 (2% in H_2 carrier gas) or B_2H_6 (2% in H_2 carrier gas) gases are used as doping sources for the doped layers. To characterize the optical properties and microstructure of the poly-SiO$_x$ materials, the intrinsic/doped a-SiO$_x$:H stack is deposited on the quartz glass substrate, as shown in Figure 1A. For passivation test, the symmetrical sample processes together with the variables are shown in Figure 1B. For both the intrinsic and doped a-SiO$_x$:H layers, the same CO_2 gas flow ratio, $R_{CO2} = [CO_2]/([CO_2]/[SiH_4])$, is used. A subsequent high-temperature annealing, operated at 850°C, is used to crystallize the materials and drive in the dopants beneath the PECVD intrinsic SiO$_x$ layer. Variable annealing time is used to optimize the passivation qualities of the poly-SiO$_x$ passivating contacts. For the double-side textured (DST) samples, the same process flow is performed with TMAH textured wafers. To improve the passivation quality of the poly-SiO$_x$ passivating contacts, the high-temperature annealed samples are capped with 75-nm-thick PECVD SiN$_x$ layer before annealing at 400°C for 30 min in 10% H_2 in N_2 atmosphere, which is normally referred as forming gas annealing (FGA). To demonstrate

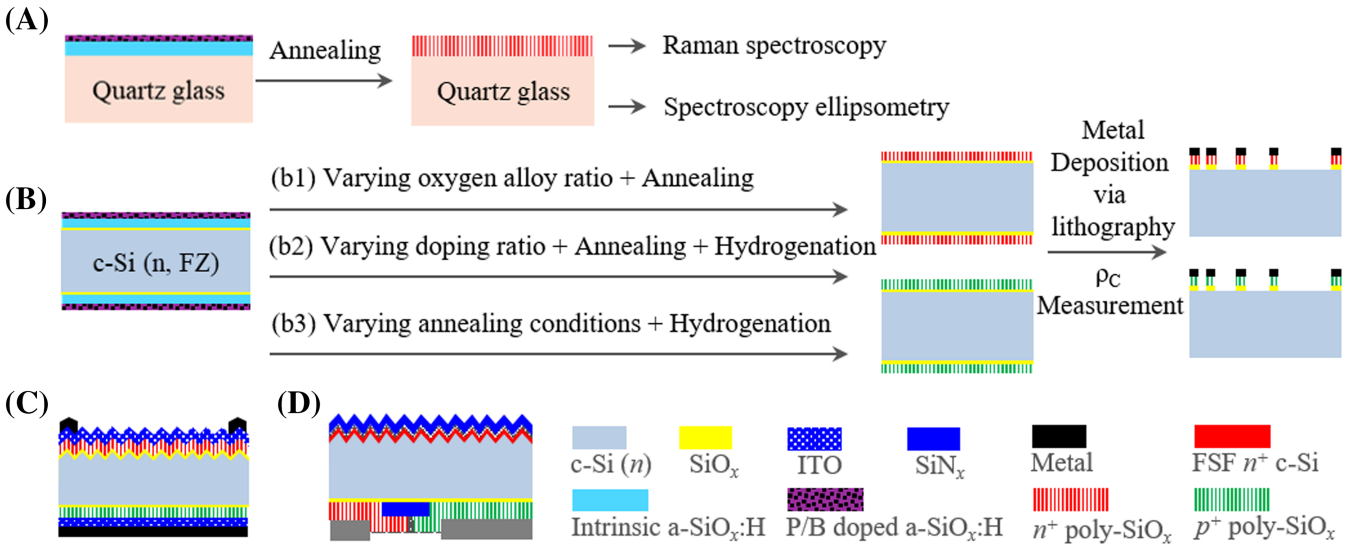

FIGURE 1 Schematic drawing of the flow to prepare poly-SiO_x samples for (A) Raman and optical measurement and (B) passivation optimization with varying oxygen content, doping level, and annealing conditions and contact resistivity measurement. (C) The sketch of a front side textured front/back-contacted (FBC) rear junction solar cells and (D) an interdigital back-contacted (IBC) solar cell with n-type and p-type poly-SiO_x passivating contacts

the application of the developed poly-SiO_x passivating contacts in solar cells, rear-junction FBC solar cells with both flat and textured n^+ poly-SiO_x on the front side and flat p^+ poly-SiO_x on the rear are prepared (see Figure 1C). At the front side of the cell, a sputtered 75-nm-thick indium tin oxide (ITO) is used as TCO and antireflection coating before the e-beam evaporated Al contacts on both sides. On the other hand, the IBC solar cell with poly-SiO_x passivating contacts (see Figure 1D) is processed with the flow as described in our previous work.[35]

The crystallinity of the poly-SiO_x material and its nanostructure are characterized with Raman spectroscopy and transmission electron microscopy (TEM), respectively. Spectroscopic ellipsometry is used to evaluate their optical properties. The transmission line method (TLM) is used to extract the contact resistivity of the SiO_x/poly-SiO_x contact stack to the c-Si bulk. The passivation qualities of the developed poly-SiO_x passivating contacts, the lifetime curves and implied open-circuit voltage (iV_{OC}), are quantified by using a Sinton WCT-120 lifetime tester applying the transient measurement mode.[46] Sinton Suns-V_{OC}-150 illumination-voltage tester is used to extract the pseudo-*FF* (*pFF*) and SunsV_{OC}. The current–voltage (I–V) performance of the solar cell is measured by using an AAA class Wacom WXS-156S-L2 solar simulator, where we obtained the solar cell parameters V_{OC}, *FF*, and $J_{SC,IV}$. External quantum efficiency (EQE) measurements were performed to evaluate wavelength-dependent optical response. The measurement is done on a special designed area aside the solar cell, where the metal fingers' spacing is large enough to fit the light spot. The $J_{SC,EQE}$ is calculated by integrating the EQE spectrum with the reference photon flux of air mass 1.5 within the wavelength range of interest (300–1200 nm). The reflectance of solar cells was also measured via the PerkinElmer Lambda 1050 system.

3 | RESULTS AND DISCUSSION

3.1 | Structural and optical properties

Alloying O into silicon film induces variation of structural, optical, and electrical properties. To study this influence on the poly-SiO_x materials, we deposited a stack of 10-nm-thick intrinsic SiO_x:H capped with 30-nm-thick n-type a-SiO_x:H layer on quartz glass substrate. Before Raman spectroscopy measurement, these samples were annealed at high temperature of 850°C for 30 min in N_2 atmosphere. The Raman crystallinity[50] of these samples with respect to the gas ratio R_{CO2} during the PECVD are shown in Figure 2A. With alloying more O within the poly-SiO_x films, the crystallinity of the annealed thin films decreases from 97% for sample with $R_{CO2} = 0$ to 35% for sample with $R_{CO2} = 0.84$. This decrease in crystalline fraction with increasing the R_{CO2} is mainly due to the formation of amorphous phase of SiO_x tissue within the polycrystalline silicon material.[36] The nanostructure of the material is evaluated by TEM with a poly-SiO_x film ($R_{CO2} = 0.62$) deposited on NAOS-SiO_x coated c-Si substrate, which underwent the same annealing as the quartz-based samples. As shown in the inset of Figure 2A, the poly-SiO_x sample with $R_{CO2} = 0.62$ shows nanometer-scale (around 10-nm) silicon crystals, which are, in most cases, contacted with each other and surrounded by the amorphous tissue. From the nanostructure point of view, because of its high crystallinity, this material is between the nanocrystalline SiO_x and the poly-Si. For sake of simplicity, we name it poly-SiO_x to simply highlight its evolution from poly-Si upon alloying with oxygen. Between the poly-SiO_x layer and the c-Si bulk, the thin NAOS–SiO_x layer is observed to be around 1.4 nm thick.

We also studied the optical properties of the poly-SiO_x films by measuring the samples with spectroscopic ellipsometry measurement.

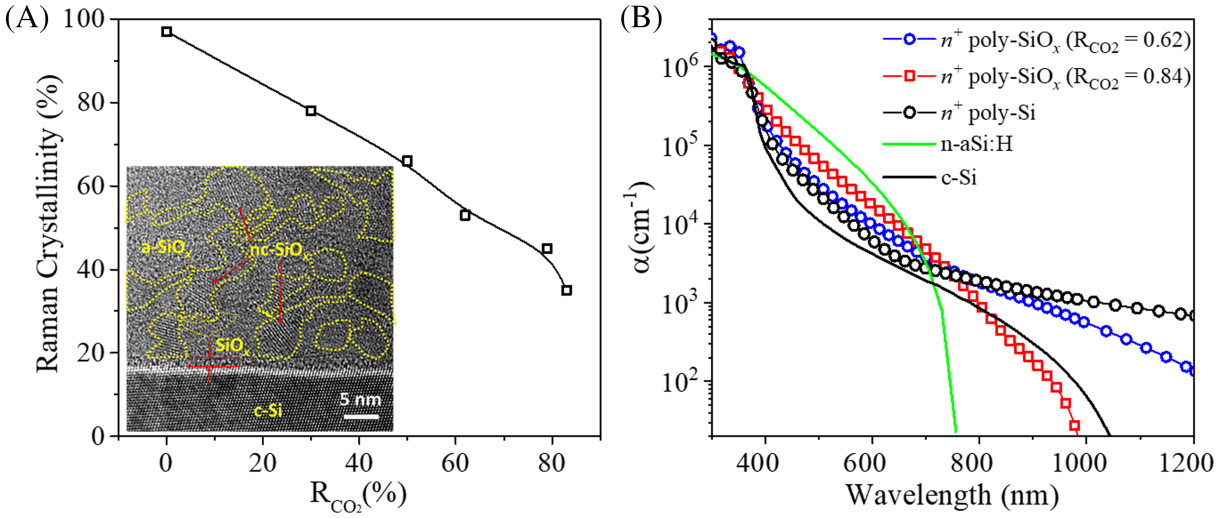

FIGURE 2 (A) The Raman crystallinity as a function of gas ratio, $R_{CO2} = [CO_2]/([CO_2]/[SiH_4])$, for n^+ poly-SiO_x samples, which were deposited on quartz glass and underwent annealing at 850°C for 30 min. The inset is a transmission electron microscopy (TEM) picture measured on sample with $R_{CO2} = 0.62$ at the poly-SiO_x/NAOS-SiO_x/c-Si interfaces. (B) The absorption coefficient (α) curves of n^+ poly-Si samples with $R_{CO2} = 0.62$ and 0.84 as a function of wavelength; the α curves related to n^+ poly-Si,[47] a-Si:H,[48] and c-Si (n)[49] are used as references

Figure 2B shows the absorption coefficient (α) curves of n^+ poly-SiO_x samples with $R_{CO2} = 0.62$ and 0.84 as a function of wavelength. The α curves of n^+ poly-Si, *n*-type a-Si:H, and *n*-type c-Si are used as references. The results are in line with those obtained with photothermal deflection spectroscopy and transmittance/reflection measurements. More details on the measurements and data fitting were presented in our previous publication.[2,38] Even though the data fitting is complicated by the mixed-phase nature of the poly-SiO_x material, we found that with increasing the oxygen alloying ratio, the absorption coefficient in the short-wavelength light region is increased with respect to that of poly-Si material. We attribute this change to the higher content of amorphous phase in the poly-SiO_x materials when increasing the oxygen content in the material, which can be seen from the Raman spectroscopy. Besides, due to such an increase, the bandgap of the poly-SiO_x material is expected to be higher. That is why we found the rapid decrease of the absorption coefficient for poly-SiO_x with $R_{CO2} = 0.84$ compared to the one with $R_{CO2} = 0.62$ and the c-Si reference, as illustrated in Figure 2B. On the other hand, we find much higher absorption coefficients for the n^+ poly-Si and poly-SiO_x with $R_{CO2} = 0.62$ at the long wavelength range with respect to the c-Si reference, which is attributed to the high FCA[38] of these two films. However, the FCA is found to be lower in the n^+ poly-SiO_x material than in n^+ poly-Si reference.

3.2 | Passivation properties

3.2.1 | Effect of the oxygen alloy ratio

We found that the amount of O alloyed within the poly-SiO_x layer plays an important role not only on the structural and optical properties but also on its passivation quality. In this work, the amount of O alloying is controlled by varying the R_{CO2} during the PECVD while keeping the rest of the deposition parameters constant. After deposition, the samples were annealed at 850°C for 30 min before the lifetime measurements. Note that this annealing condition might not be the optimum for all the samples with different O alloy ratio. No hydrogenation processes were applied so far on these samples. The effective lifetime curves of both n^+ poly-SiO_x on DST wafers and p^+ poly-SiO_x DSP wafers as function of R_{CO2} values are shown in Figure 3A,B, respectively. In general, with increasing the R_{CO2}, the passivation quality decreases in both n^+ and p^+ poly-SiO_x samples. For DST n^+ poly-SiO_x, samples with lower R_{CO2} (≤0.62) show much higher passivation quality compared to the samples with higher R_{CO2} (≥0.71). For DSP p^+ poly-SiO_x samples, when R_{CO2} is in the range of [0.55, 0.71], the iV_{OC} values are at ~673 mV. Like n^+ poly-SiO_x, a higher R_{CO2} induces a lower passivation quality in p^+ poly-SiO_x, while lower R_{CO2} values (≤0.38) results in better passivation. We attribute the dependence of the passivation quality on the R_{CO2} values to the active doping level of the poly-SiO_x materials. The profile of the active dopants within the poly-SiO_x contacts could not be accurately measured by our electrochemical capacitance-voltage (ECV) setup due to the uneven etching behavior by the currently used etchant. However, at a certain point when the poly-SiO_x was completely etched, the doping level of the c-Si surface region was detectable. We found for n^+ poly-SiO_x samples with $R_{CO2} = 0.83$ one order of magnitude lower phosphorus concentration than for the samples with $R_{CO2} = 0.50$, indicating a lower phosphorus concentration within the n^+ poly-SiO_x for $R_{CO2} = 0.83$ sample. This is in line with our previous studies on the a-SiO_x:H thin film materials; with the increase of the O alloy ratio in the silicon films, their conductivity decreases, which indicates a lower doping level in the film.[51,52] When deploying the poly-SiO_x films

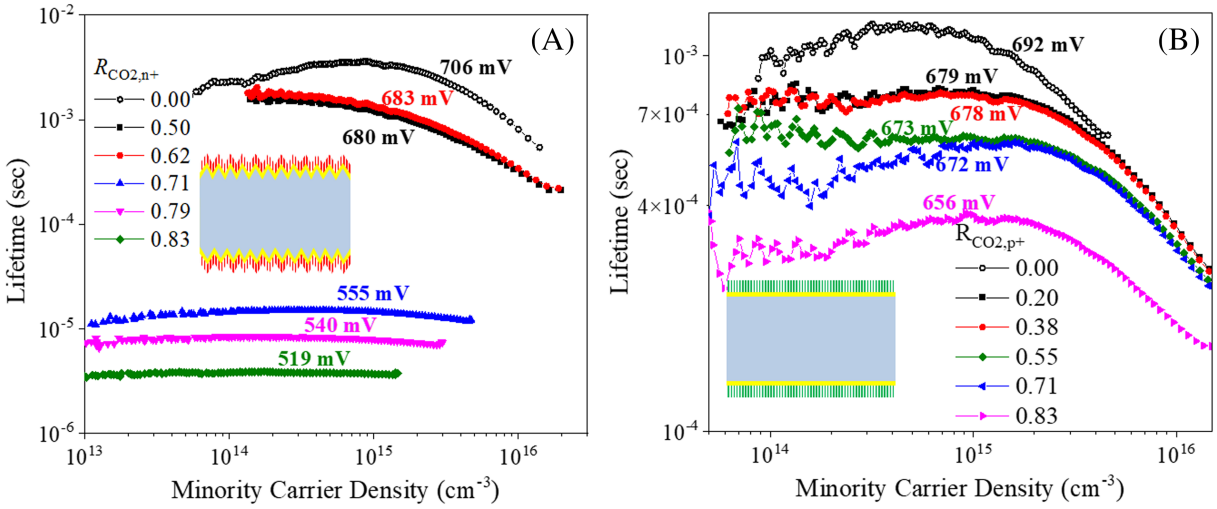

FIGURE 3 Effective lifetime of the symmetrical test samples, prepared with variable R_{CO2}, as a function of minority carrier density for both (A) n^+ poly-SiO_x prepared on DST c-Si wafers and (B) p^+ poly-SiO_x prepared on DSP c-Si wafers. The measured results shown here are related to samples without hydrogenation

as passivating contacts, the higher the doping level in the poly-SiO_x films is, the stronger the induced electrical field is, resulting in improved passivation. However, according to the optical measurement of the poly-SiO_x layers, to achieve device-level optical quality the chosen R_{CO2} value should be high enough to minimize the absorption coefficient.[38] Therefore, taking the passivation quality and the optical properties into consideration, we select $R_{CO2} = 0.62$ and 0.55 for preparing n^+ and p^+ poly-SiO_x passivating contacts, respectively, in the following sections of this work.

3.2.2 | Influence of doping ratio

For passivating contacts based on poly-Si alloy, the doping level within the poly-Si alloy layer and the doping profile across the poly-Si alloy/SiO_x/c-Si interface are the main factors influencing the quality of the field-effect passivation.[53] There are some parameters that can control the doping level and profile for such PECVD prepared passivating contacts: (i) the phosphorus or boron content in the PECVD a-SiO_x:H layers, (ii) the thicknesses of the intrinsic and doped PECVD a-SiO_x:H layers, (iii) the thermal budget of high-temperature annealing process, and (iv) the thickness and quality of the ultrathin SiO_x layers. In this work, the effect of these parameters, namely, the influence of the PECVD a-SiO_x:H layers doping level and the high-temperature annealing on the poly-SiO_x passivating contact passivation quality, will be discussed in the following sections.

Because of the bilayer approach (10 nm thick intrinsic coated with doped a-SiO_x layers) used in this work when preparing the poly-SiO_x passivating contacts, the doping level can be modified by varying the doping concentration and thickness of the doped a-SiO_x:H layer during the PECVD. During the a-SiO_x:H deposition, the doping is controlled by varying the doping gas flow ratio, R_{doping}, which is defined as $R_{doping} = [\text{doping gas}]/([\text{doping gas}] + [SiH_4])$, while the thicknesses of *n*-type and *p*-type doped a-SiO_x:H are fixed to be 20 and 10 nm thick, respectively. The effect of R_{doping} on the passivation quality of the poly-SiO_x passivating contacts is shown in Figure 4A. For both n^+ and p^+ poly-SiO_x passivating contacts, their passivation properties first increase and then decrease with increasing the doping level of the PECVD doped layers. It means that there is an optimum R_{doping} for both DST n^+ and DSP p^+ poly-SiO_x passivating contacts. On the other hand, when fixing the optimum R_{doping} for both *n*-type and *p*-type a-SiO_x:H layers, while only varying the thicknesses of the doped layer, we find that there is a minimum thickness to obtain the maximum passivation quality. A too thick doped layer leads to lower passivation quality, as shown in Figure 4B. We observe that when the amount of dopants in the doped a-SiO_x:H layer is too low (whether too low R_{doping} or too thin doped layers), the passivation worsens. We speculate that the doping concentration differences at the poly-SiO_x/SiO_x/c-Si interfaces is not high enough to induce a strong field-effect passivation at these interfaces. On the contrary, when the amount of dopants within the a-SiO_x:H layers is too high (whether too high R_{doping} or too thick doped layers), the following high-temperature annealing will drive a too high amount of dopants inside the c-Si bulk through the NAOS–SiO_x. This induces high Auger recombination beneath the surface region of the c-Si wafer and decreases the doping concentration differences at the poly-SiO_x/SiO_x/c-Si interfaces, which weakens the field-effect passivation. These two facts affect the overall passivation quality of the poly-SiO_x passivating contacts.

3.2.3 | Influence of the high-temperature annealing

The results discussed in the previous sections provide, by modifying the doping processes, guidelines for optimizing the deposition conditions of the DST and DSP n^+ and DSP p^+ poly-SiO_x passivating contacts. In this section, we studied the influence of the high-

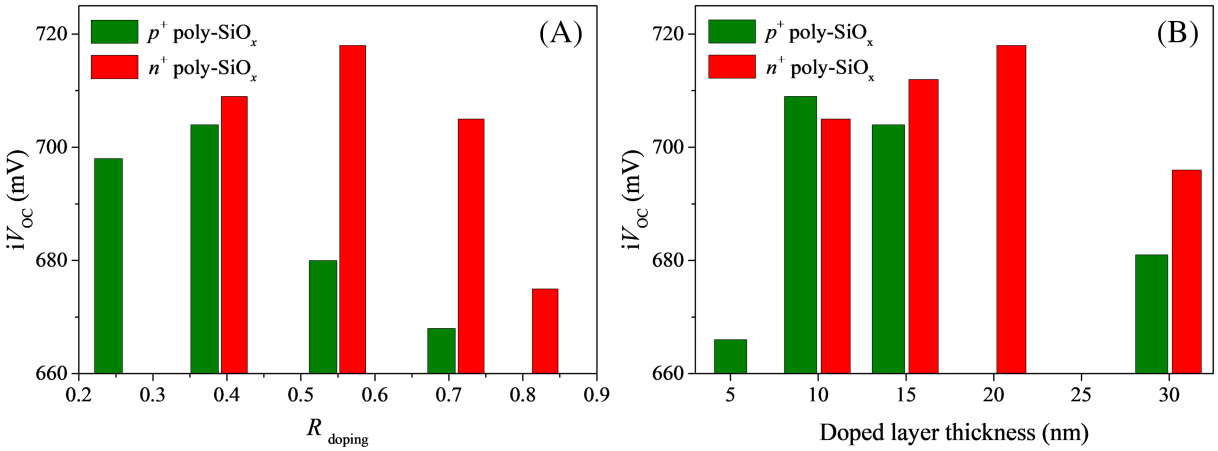

FIGURE 4 The measured iV_{OC}s of the poly-SiO$_x$ symmetric test samples as a function of (A) the doping ratio of the PECVD doped a-SiO$_x$:H layers, R_{doping} (R_{doping} = [doping gas]/([doping gas] + [SiH$_4$])), for both DST n$^+$ and DSP p$^+$ poly-SiO$_x$ passivating contacts. The intrinsic a-SiO$_x$:H layers used in these samples are 10 nm thick, while the thicknesses for n-type and p-type doped a-SiO$_x$:H layers are 20 and 10 nm thick, respectively; and (B) the thickness of the PECVD doped a-SiO$_x$:H layers, when the thickness of the intrinsic a-SiO$_x$:H is fixed to 10 nm, and the R_{doping} is set to 0.62 and 0.40 for n-type and p-type a-SiO$_x$:H layers, respectively. All the passivation results shown here are measured after hydrogenation with 75-nm-thick PECVD SiN$_x$ capping which is followed by FGA at 400°C for 30 min

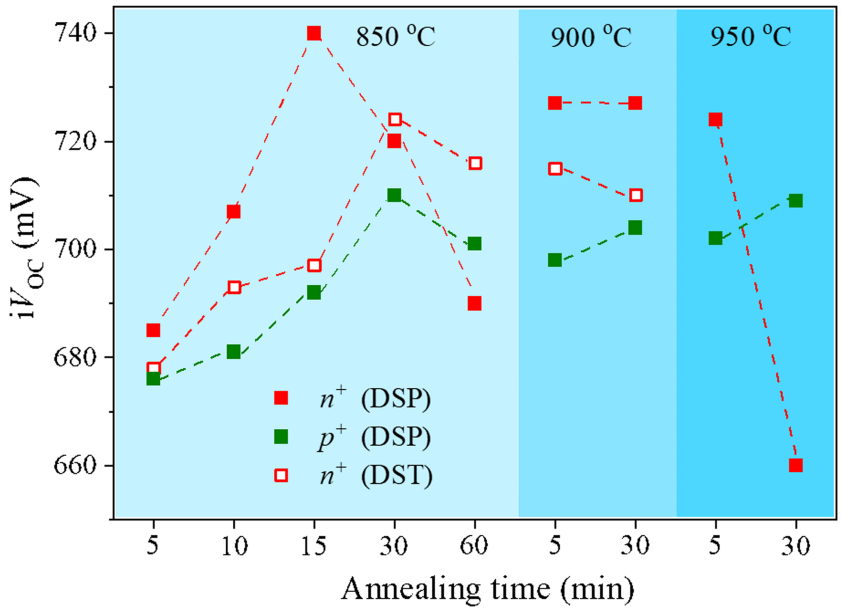

FIGURE 5 The iV_{OC} values as a function of the annealing time at 850, 900 and 950°C for both DSP and DST n$^+$ and DSP p$^+$ poly-SiO$_x$ symmetric test samples. The optimum doping ratio and thickness of the doped layer obtained from Figure 4 are applied here. All the passivation results shown here are measured after hydrogenation with 75-nm-thick PECVD SiN$_x$ capping which is followed by FGA at 400°C for 30 min

temperature annealing time on the passivation quality for these poly-SiO$_x$ passivating contacts. After high-temperature annealing, the samples were hydrogenated by 75-nm-thick PECVD SiN$_x$ capping which was followed by FGA at 400°C for 30 min before lifetime measurements. The iV_{OC} values are shown in Figure 5. For both the DSP n^+ and p^+ poly-SiO$_x$ passivating contacts, we observe an optimal annealing time of 15 and 30 min at 850°C annealing temperature that maximizes the iV_{OC} to 740 and 709 mV, respectively. The high-temperature annealing step is used to crystalize both the intrinsic and doped a-SiO$_x$:H layer and diffuse the dopants from in situ doped a-SiO$_x$:H layer into the intrinsic layer to form a uniformly doped poly-SiO$_x$. If the annealing time is too short, the dopants do not receive enough energy to diffuse through the intrinsic poly-SiO$_x$ layer; therefore, the doping profile is expected to be very shallow within the poly-SiO$_x$ material. On the other hand, if the annealing time is too long or the temperature is too high, more dopants are expected to diffuse through the intrinsic and the NAOS-SiO$_x$ layers into the c-Si bulk to form a deep junction within the c-Si bulk. As discussed in section 3.2.1, the doping level of the poly-SiO$_x$ layer could not be extracted by our ECV measurements. However, both cases are expected to lead to low passivation qualities due to the weakening of field-effect passivation at the c-Si/NAOS-SiO$_x$/(doped) poly-SiO$_x$ interfaces and/or the enhanced Auger recombination within the bulk. Similar to the poly-Si case,[6] an optimal passivation quality requires a doping profile that has

a sharp doping level drop at the c-Si surface at the c-Si/NAOS-SiO_x/(doped) poly-SiO_x interfaces, which induces a strong electrical field at this interface, therefore enhancing the passivation quality. Results show that the optimal time of annealing temperature leads to such an optimal doping profile. In this work, based on the n^+ poly-SiO_x results shown in Figure 5, it is found that the optimum annealing time for textured samples is longer than that for flat samples. We speculate that the difference between polished and textured samples is due to the NAOS–SiO_x layer property differences when grown on the polished <100> and textured <111> c-Si surfaces.[54] Interestingly, for the DSP p^+ poly-SiO_x, the same optimum annealing time as DST n^+ poly-SiO_x is observed. Accordingly, we can integrate at device level both layers sharing the same optimal annealing time.

3.3 | Contact resistivity and solar cell performance

Before applying the developed poly-SiO_x passivating contacts into c-Si solar cells, we measured the contact resistivity (ρ_C) of the optimum passivating contact stack to the c-Si bulk via TLM. The measured ρ_c of the samples together with corresponding passivation performances of these samples are listed in Table 1. For both n^+ and p^+ poly-SiO_x passivating contacts, ρ_C values below 1 mΩ/cm^2 are obtained. As the annealing temperature of 850°C is relatively low for this technology of passivating contacts, we did not observe pinholes at the NAOS-SiO_x layer in any of the 40 TEM images that were made on n^+ poly-SiO_x samples. Therefore, we expect that the obtained low ρ_c values indicate good tunneling of carriers through the NAOS-SiO_x layer. Besides, these ρ_C values are at the same level as our previously developed ion-implanted LPCVD poly-Si passivating contacts (see Table 1), which led to IBC solar cell *FF* of 81%.[55] Considering the similar passivation and contact resistivity characteristics of the poly-SiO_x as the poly-Si passivating contacts, we anticipate similar carrier collection behavior by these two kinds of passivating contacts.

We firstly fabricated double-side flat FBC solar cell with ITO on both sides. As shown in Table 2, this cell achieves a *FF* as high as 83.5%, which proves an effective carrier collection by the poly-SiO_x passivating contacts. However, the co-annealing of the poly-SiO_x is done at 850°C for 30 min. This condition ensures the flat p^+ poly-Si performs the best at the expenses of the flat n^+ poly-SiO_x. Therefore, after finalizing the cell with ITO and metal, the cell exhibited a V_{OC} of only 681 mV. With the same process condition, when the front side is replaced with n^+ poly-SiO_x deposited on textured c-Si surface, which performs a better passivation than the flat one with the same annealing condition, an iV_{OC} of 707 mV was measured after hydrogenation with SiN_x capping and FGA. After the SiN_x capping was

TABLE 1 The best passivation properties of poly-SiO_x passivating contacts on symmetrical samples and measured contact resistivity (ρ_C) extracted from TLM of e-beam evaporated aluminum/poly-SiO_x/NAOS-SiO_x contacts to c-Si bulk

		Passivating contact				Passivation		Contact
Nr.	Base Si	Growth	Doping	Type	Thickness [nm]	J_0 (fA/cm^2)	iV_{OC} (mV)	ρ_C (mΩ/cm^2)
1	n-FZ, DSP	PECVD	In situ, B	p^+ poly-SiO_x	20	16	709	27
2	n-FZ, DSP	PECVD	In situ, P	n^+ poly-SiO_x	35	3.0	740	18
3	n-FZ, DST	PECVD	In situ, P	n^+ poly-SiO_x	35	11.0	718	23
4[a]	n-FZ, DSP	LPCVD	B implantation	p^+ poly-Si	250	11	716	24
5[a]	n-FZ, DSP	LPCVD	P implantation	n^+ poly-Si	250	4.5	735	13

Note: The ion-implanted poly-Si passivating contacts from ref.[55] are also listed as reference.
[a]Ion-implanted LPCVD poly-Si passivating contacts with doping activation at a temperature of 950°C.

TABLE 2 Performance of FBC and IBC solar cells with poly-SiO_x passivating contact

Solar cell	Passivating contacts	Area (cm^2)	V_{OC} (mV)	$J_{SC,IV}$[a] (mA/cm^2)	$J_{SC,EQE}$ (mA/cm^2)	*FF* (%)	η (%)
FBC (DSP, best cell)	Poly-SiO_x	2	681	33.4	34.5	83.5	19.6[b]
FBC (front tex.) (avg.)	Poly-SiO_x	2	688 ± 3	38.9 ± 0.3		76.1 ± 0.5	20.5 ± 0.4
FBC (front tex.) (best)	Poly-SiO_x	2	691	39.3	39.7	76.4	21.0[b]
Ref. FBC (front tex.)[c]	Poly-Si	2	668 ± 3	38.0 ± 0.1	38.0	78.6 ± 0.4	20.0 ± 0.2
IBC (front tex.)	Poly-SiO_x	9	650	39.3	~	77.0	19.7
Ref. IBC[55]	Poly-Si	1	682	41.6	~	81.0	23.0

Notes: Results of FBC and IBC solar cells with ion-implanted LPCVD poly-Si passivating contacts[7] are also listed as references in the table. For the FBC cells, the average results are based on three different solar cells.
[a]Busbars on the four edges of the cell are not illuminated.
[b]The efficiency is calculated with $J_{SC,EQE}$.
[c]Front-side textured FBC cell with ~20 nm n^+ poly-Si on the front side and 250 nm p^+ poly-Si on the rear side.[56]

removed with BHF (1:7), the iV_{OC} drops to 699 mV. A further decrease to 695 mV was observed after ITO sputtering due to the sputtering damage. After the deposition of the e-beam evaporated Al, due to the exposure to the e-beam radiation, the final cell V_{OC} of 691 mV was achieved. On the other hand, compared to the double-side flat solar cell, the solar cell *FF* drops to 76.4%. Considering the similar *pFFs*, ~84%, measured for both double-side flat and front-side textured cells, we attribute this drop in *FF* mainly to the resistive loss from the metal fingers, which is e-beam evaporated Al on the textured Si surface. With the same evaporation process, the thickness of Al finger on the textured surface facades is ~1.2 μm, which is 1.7 times thinner than that deposited on the flat surface (~2 μm). We compared this solar cell to an FBC cell based on poly-Si with similar cell structure but different in the thicknesses of the passivating contact layers: 20-nm-thick n^+ poly-Si on the front textured surface which is covered with an ITO layer and 250-nm-thick p^+ poly-Si on the flat rear side which was contacted by ITO/Ag.56 Due to the thinner poly-Si layer on the front side, the backend metallization processes induced a higher V_{OC} loss which led to a lower V_{OC} for the poly-Si cell with respect to the poly-SiO_x cell. From an optical point of view, even though the 35-nm-thick n^+ poly-SiO_x layer used at the front side is thicker than the 20-nm-thick n^+ poly-Si in the FBC cells, the final $J_{SC,IV}$ of the FBC cells based on poly-SiO_x is ~1.3 mA/cm^2 higher than that of the cells based on poly-Si. These two results indicate the optical and the carriers collection advantages of poly-SiO_x compared to thin poly-Si passivating contacts when used in the solar cells. To address the optical performance of poly-SiO_x passivating contacts when applied on solar cells, we measured the EQE and the reflectance of the front-side textured FBC solar cell, see Figure 6. We observe that the n-type poly-SiO_x passivating contact together with the ITO layer, which yields a parasitic loss in photogenerated current density within the c-Si bulk of around 1.40 mA/cm^2, induces some parasitic absorption at short wavelengths otherwise minimal in a PERC cell.[57] Nevertheless, a high $J_{SC,EQE}$ of 39.7 mA/cm^2 was achieved, resulting in a cell efficiency of 21.0%. This front textured FBC solar cell endowed with poly-SiO_x passivating contacts exhibits an illuminated area $J_{SC,IV}$ value (39.3 mA/cm^2) that is in the same range of that reported for state-of-the-art, large-area, double-side textured, low-thermal budget classical heterojunction (39.5 mA/cm^2).[58] This result puts well in perspective the optical potential of poly-SiO_x passivating contacts.

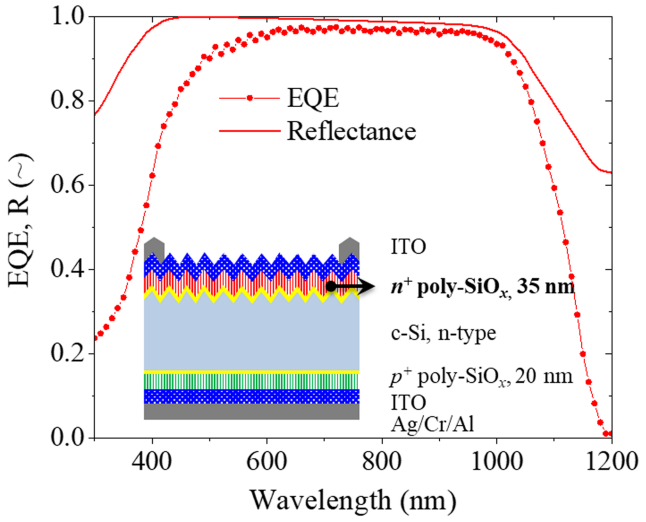

FIGURE 6 The EQE and the reflectance curves of FBC solar cells with poly-SiO_x as passivating contacts for both polarizations. Inset: The sketches for solar cell with poly-SiO_x as passivating contacts. The n^+ poly-SiO_x and p^+ poly-SiO_x are 35 and 20 nm thick, respectively. The FBC cell also features 75-nm- and 120-nm-thick ITO layers on the front and rear side, respectively. The $J_{SC,EQE}$ computed from the EQE spectrum is 39.7 mA/cm^2

Considering the short-wavelength-range parasitic absorption of poly-SiO_x layers when used at the front side of the cell, the best approach to apply both n^+ and p^+ poly-SiO_x passivating contacts in one solar cell is to deploy the IBC solar cell architecture. Since the rear side of an IBC device is hardly reached by short-wavelength light, the optical potential of both n^+ and p^+ poly-SiO_x passivating contacts placed there could be exploited. Following the process flow described in our previous work,[35] IBC solar cell based on poly-SiO_x passivating contacts with efficiency of 19.7% is manufactured, as sketched in Figure 7A. In this work, we compare its optical performance to that obtained by the reference IBC cell featuring passivating contacts based on poly-Si,[55] as depicted in Figure 7B. The performances of both IBC cells are listed in Table 2. Due to the not yet optimized gap isolation between n^+ and p^+ poly-SiO_x fingers, the V_{OC} is limited to only 650 mV by the recombination, which hinders cell's overall performance, especially its spectral response. Comparing the IQE curves of poly-SiO_x IBC to the poly-Si IBC, this recombination loss is considered as the main reason for the lower IQE values in the wavelength shorter than 1100 nm. However, a higher IQE is observed at long wavelengths (>,100 nm) for cells with poly-SiO_x passivating contacts than in case of IBC cells with poly-Si ones, as reported in Figure 7C. We attribute this IQE gain to the higher transparency of the poly-SiO_x passivating contacts in that wavelength range. In fact, for these two IBC cell architectures, long-wavelength photons reaching the rear passivating contacts will be (i) partly absorbed by the passivating contacts, (ii) partly absorbed by the metal at the passivating contact/Al interface, and (iii) partly reflected from the rear contact interfaces. Due to the lower absorption coefficient of the poly-SiO_x than poly-Si, the parasitic absorption by the poly-SiO_x passivating contacts is expected to be lower than that by the poly-Si ones. Besides that, a lower reflective index of the poly-SiO_x layers[38] than poly-Si also enhances the light reflection at their interfaces into the c-Si bulk, minimizing the chances that light is absorbed by the passivating contacts. At the rear of poly-Si IBC solar cells, there is a SiN_x spacing layer between metal contact and the poly-Si layers with an area coverage of 75%. It increases the light reflection at its interfaces to the poly-Si and bulk, which can be seen from the higher R values of the solar cell, shown in Figure 7C. However, the enhanced light reflection also enhances the absorption of poly-Si passivating contacts, when considering the much higher absorption of the poly-Si than c-Si bulk. Due to

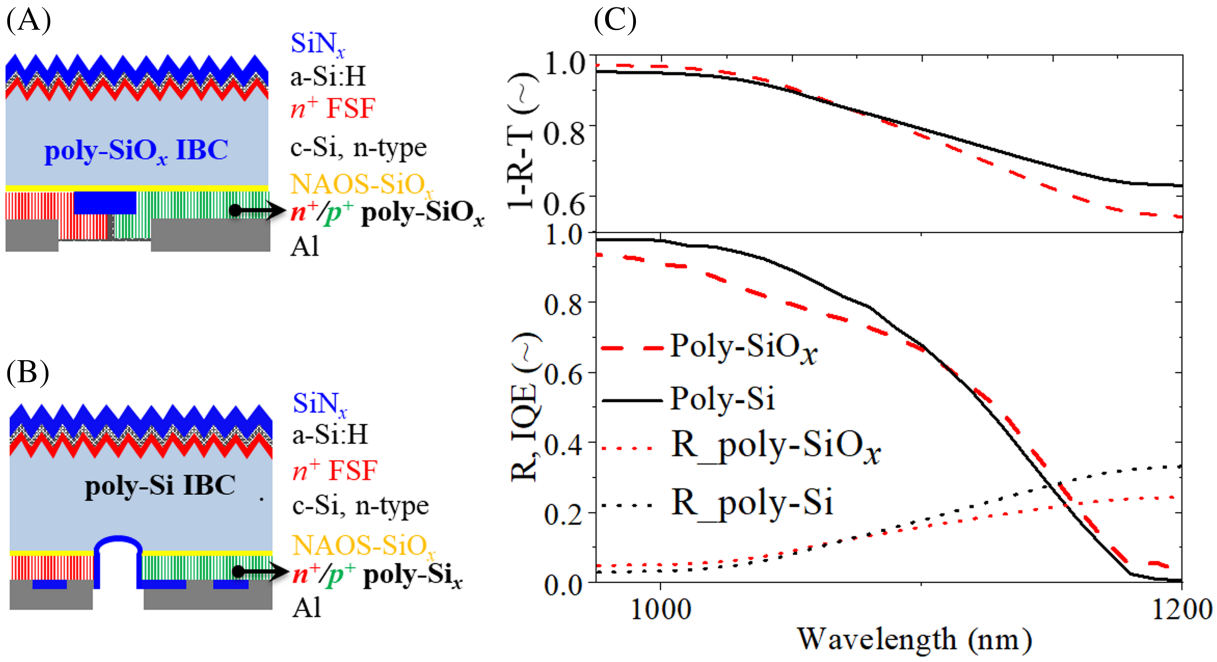

FIGURE 7 IBC solar cell sketches featuring (A) doped poly-SiO_x or (B) doped poly-Si as passivating contacts. (C) The internal quantum efficiency (IQE) of both IBC solar cells. The diagram (C) zooms on the long wavelength range of the IQE curve and of reflectance (R) and transmittance (T) spectra, which are plotted as *1-R-T*. The process of the solar cell are presented in our previous work[7,55]

the same metal finger design for both cells, the transmittance (*T*) of the cell through the metal finger gaps is the same. Therefore, a lower *1-R-T* spectrum is observed in the poly-SiO_x IBC cell in the wavelength range above 1100 nm than that for poly-Si IBC cell, which enhances the light absorption in the bulk, as shown in Figure 7C. As a consequence, within this wavelength range, a higher IQE spectrum is observed for poly-SiO_x IBC cell with respect to that of the poly-Si IBC cell. By optimizing the patterning process of IBC solar cells based on poly-SiO_x passivating contacts, an overall higher EQE response is expected with respect to the IBC cells based on poly-Si passivating contacts.

4 | CONCLUSIONS

In this work, we presented the optimization and characterization of carrier-selective passivating contact based on doped poly-SiO_x. Their optical and electrical behavior when applied in both FBC and IBC c-Si solar cells is examined. The poly-SiO_x material is a mixed-phase material with nanometer-scale Si crystals. The nanostructure is found to be closely related to the PECVD parameters, especially the amount of oxygen alloy ratio. To achieve excellent passivation and carrier selectivity, we found that there is an optimum PECVD process window on the oxygen alloy ratio and doping ratio for poly-SiO_x passivating contacts. For both n^+ and p^+ poly-SiO_x passivating contacts, outstanding passivation qualities ($iV_{OC,flat,n+} = 740$ mV; contact resistance $\rho_c = 0.7$ mΩ/cm^2; $iV_{OC,flat,p+} = 709$ mV; $\rho_c = 0.5$ mΩ/cm^2) are achieved by optimizing the deposition, post-annealing, and the hydrogenation processes. Besides the low contact resistivity, the high cell *FF* of 83.5% obtained in double-side flat FBC solar cells with poly-SiO_x as both polarities indicates their highly efficient carrier collection capability. Optically, due to the bandgap widening induced by O alloying, the absorption coefficient of poly-SiO_x becomes lower than that of poly-Si passivating contacts at long wavelengths. This optical advance of poly-SiO_x against poly-Si as passivating contact is also demonstrated at solar cell level in a 21.0% FBC solar cell and in a 19.7% IBC cell with higher long-wavelength IQE response compared to the reference poly-Si IBC cell with similar cell structure.

ACKNOWLEDGEMENT

This work was performed in the project HT-SOHO (TEUE117010) and SATURNIA (TEUE118002), which received funding from the Topsector Energie of the Dutch Ministry of Economic Affairs.

DATA AVAILABILITY STATEMENT

The data that support the findings of this study are available from the corresponding author upon reasonable request.

ORCID

Guangtao Yang https://orcid.org/0000-0001-8288-7394
Can Han https://orcid.org/0000-0002-3213-6856
Paul Procel https://orcid.org/0000-0003-4997-3551
Yifeng Zhao https://orcid.org/0000-0003-3789-5090
Luana Mazzarella https://orcid.org/0000-0001-8320-8103
Miro Zeman https://orcid.org/0000-0002-1710-360X
Olindo Isabella https://orcid.org/0000-0001-7673-0163

REFERENCES

1. Haase F, Hollemann C, Schäfer S, et al. Laser contact openings for local poly-Si-metal contacts enabling 26.1%-efficient POLO-IBC solar cells. *Sol Energy Mater sol Cells*. 2018;186:184-193.
2. Feldmann F, Bivour M, Reichel C, Steinkemper H, Hermle M, Glunz SW. Tunnel oxide passivated contacts as an alternative to partial rear contacts. *Sol Energy Mater sol Cells*. 2014;131(PART A):46-50.
3. Duttagupta S, Nandakumar N, Padhamnath P, Buatis JK, Stangl R, Aberle AG. monoPoly™ cells: large-area crystalline silicon solar cells with fire-through screen printed contact to doped polysilicon surfaces. *Sol Energy Mater Sol Cells*. 2018;187:76-81.
4. Richter A, Benick J, Feldmann F, Fell A, Hermle M, Glunz SW. n-Type Si solar cells with passivating electron contact: identifying sources for efficiency limitations by wafer thickness and resistivity variation. *Sol Energy Mater Sol Cells*. 2017;173:96-105.
5. Yan D, Cuevas A, Bullock J, Wan Y, Samundsett C. Phosphorus-diffused polysilicon contacts for solar cells. *Sol Energy Mater Sol Cells*. 2015;142:75-82.
6. Yang, Ingenito A, Isabella O, Zeman M. IBC c-Si solar cells based on ion-implanted poly-silicon passivating contacts. *Sol Energy Mater Sol Cells*. 2016;158:84-90.
7. Yang G, Guo P, Procel P, Weeber A, Isabella O, Zeman M. Poly-crystalline silicon-oxide films as carrier-selective passivating contacts for c-Si solar cells. *Appl Phys Lett*. 2018;112(19):1-6.
8. Kim H, Bae S, Ji KS, et al. Passivation properties of tunnel oxide layer in passivated contact silicon solar cells. *Appl Surf Sci*. 2017;409:140-148.
9. Gao T, Yang Q, Guo X, et al. An industrially viable TOPCon structure with both ultra-thin SiOx and n+-poly-Si processed by PECVD for p-type c-Si solar cells. *Sol Energy Mater Sol Cells*. 2019;200:109926.
10. Tachibana T, Tanahashi K, Mochizuki T, Shirasawa K, Takato H. Bifacial interdigitated-back-contact (IBC) crystalline silicon solar cell: fabrication and evaluation by internal quantum efficiency mapping. 2018 IEEE 7th World Conf. Photovolt. Energy Conversion, WCPEC 2018 - A Jt. Conf. 45th IEEE PVSC, 28th PVSEC 34th EU PVSEC, no. Step 4, pp. 3738-3742; 2018.
11. Römer U, Peibst R, Ohrdes T, et al. Ion implantation for poly-Si passivated back-junction back-contacted solar cells. *IEEE J Photovolt*. 2015;5(2):507-514.
12. Allebe C, Leon JJD, Ingenito A, et al. PECVD based layers for improved high temperature industrial Solar cell processes. *IEEE J. Photovolt*. 2020:2196-2199.
13. Nandakumar N, Rodriguez J, Kluge T, et al. Approaching 23% with large-area monoPoly cells using screen-printed and fired rear passivating contacts fabricated by inline PECVD. *Prog Photovoltaics Res Appl*. 2019;27(2):107-112.
14. Stodolny MK, Anker J, Geerligs BLJ, et al. Material properties of LPCVD processed n-type polysilicon passivating contacts and its application in PERPoly industrial bifacial solar cells. *Energy Procedia*. 2017;124:635-642.
15. Stradins P, Essig S, Nemeth W, et al. Passivated tunneling contacts to N-type wafer silicon and their implementation into high performance solar cells preprint. 6th World Conf. Photovolt. Energy Convers., pp. 3-6; 2014.
16. Park H, Park H, Park SJ, et al. Passivation quality control in poly-Si/SiOx/c-Si passivated contact solar cells with 734 mV implied open circuit voltage. *Sol Energy Mater Sol Cells*. 2019;189:21-26.
17. Zhang Z, Zeng Y, Jiang CS, et al. Carrier transport through the ultrathin silicon-oxide layer in tunnel oxide passivated contact (TOPCon) c-Si solar cells. *Sol Energy Mater Sol Cells*. 2018;187:113-122.
18. Chen Y, Chen D, Liu C, et al. Mass production of industrial tunnel oxide passivated contacts (i-TOPCon) silicon solar cells with average efficiency over 23% and modules over 345 W. *Prog Photovoltaics Res Appl*. 2019;27(10):827-834.
19. Chen J. The Industrial Application of n-type Bifacial Passivating-contact Technology. *9th Int*. Conf. Cryst. Silicon Photovoltaics; 2019.
20. JinkoSolar large-area N-type monocrystalline silicon solar cell reaches record high efficiency of 24.79%. 2020 Press Releases by Jinko Solar. 2020. https://ir.jinkosolar.com/news-releases/news-release-details/jinkosolar-large-area-n-type-monocrystalline-silicon-solar-cell
21. Yang Y. Recent progress at Trina in large area IBC cells with passivated contacts. *8th Int*. Conf. Cryst. Silicon Photovoltaics; 2018.
22. Canadian Solar sets a 22.80% conversion efficiency world record for P-type large area multi-crystalline silicon solar cell. 09/17/2019 Press Release, CanadianSolar. http://investors.canadiansolar.com/news-releases/news-release-details/canadian-solar-sets-2280-conversion-efficiency-world-record-p
23. Canadian Solar sets a 23.81% conversion efficiency world record for N-type large area multi-crystalline silicon solar cell. 03/06/2020 Press Release, CanadianSolar. http://investors.canadiansolar.com/news-releases/news-release-details/canadian-solar-sets-2381-conversion-efficiency-world-record-n
24. Richter A, Müller R, Benick J, et al. Design rules for high-efficiency both-sides-contacted silicon solar cells with balanced charge carrier transport and recombination losses. *Nat Energy*. 2021;6:429-438.
25. Limodio G, Yang G, de Groot Y, et al. Implantation-based passivating contacts for crystalline silicon front/rear contacted solar cells. *Prog Photovoltaics Res Appl*. 2020;28:403-416.
26. Ingenito A, Nogay G, Jeangros Q, et al. A passivating contact for silicon solar cells formed during a single firing thermal annealing. *Nat Energy*. 2018;3(9):800-808.
27. Nogay G, Ballif C, Ingenito A, et al. Crystalline silicon solar cells with coannealed electron- and hole-selective SiC x passivating contacts. *IEEE J. Photovoltaics*. 2018;8(6):1478-1485.
28. Feldmann F, Reichel C, Müller R, Hermle M. The application of poly-Si/SiOx contacts as passivated top/rear contacts in Si solar cells. *Sol Energy Mater Sol Cells*. 2017;159:265-271.
29. Reiter S, Koper N, Reineke-Koch R, et al. Parasitic absorption in poly-crystalline Si-layers for carrier-selective front junctions. *Energy Procedia*. 2016;92:199-204.
30. Feldmann F, Reichel C, Müller R, Hermle M. Si solar cells with top/-rear poly-Si contacts. 2016 IEEE 43rd Photovoltaic Specialists Conference, pp. 2421-2424; 2016.
31. Stuckelberger J. Transparent passivating contacts for front side application in crystalline silicon solar cells. PhD Thesis. École polytechnique fédérale de Lausanne; 2018.
32. Christoph Messmer MH, Fell A, Feldmann F, Schon J. Upgrade PERC with TOPCon: efficiency potential by taking into account the electrical gains and optical losses. 36th Eur. Photovolt. Sol. Energy Conf. Exhib.; 2019.
33. Ingenito A, Limodio G, Procel P, et al. Silicon solar cell architecture with front selective and rear full area ion-implanted passivating contacts. *Sol RRL*. 2017;1(7):1700040.
34. Ingenito A, Nogay G, Stuckelberger J, et al. Phosphorous-doped silicon carbide as front-side full-area passivating contact for double-side contacted c-Si solar cells. *IEEE J Photovoltaics*. 2019;9(2):346-354.
35. Yang G, Zhang Y, Procel P, Weeber A, Isabella O, Zeman M. Poly-Si (O)x passivating contacts for high-efficiency c-Si IBC solar cells. *Energy Procedia*. 2017;124:392-399.
36. Stuckelberger J, Nogay G, Wyss P, et al. Passivating electron contact based on highly crystalline nanostructured silicon oxide layers for silicon solar cells. *Sol Energy Mater Sol Cells*. 2016;158:2-10.
37. Pomaska M, Köhler M, Procel Moya P, et al. Transparent silicon carbide/tunnel SiO2 passivation for c-Si solar cell front side: enabling Jsc > 42 mA/cm2 and iVoc of 742 mV. *Prog Photovoltaics Res Appl*. 2020;28:321-327.
38. Singh M, Santbergen R, Mazzarella L, et al. Optical characterization of poly-SiOx and poly-SiCx carrier-selective passivating contacts. *Sol Energy Mater Sol Cells*. 2020;210:110507.

39. Wyss P, Stuckelberger J, Nogay G, et al. A mixed-phase SiOx hole selective junction compatible with high temperatures used in industrial solar cell manufacturing. *IEEE J Photovoltaics*. 2020;10(5):1262-1269.
40. Mack I, Stuckelberger J, Wyss P, et al. Properties of mixed phase silicon-oxide-based passivating contacts for silicon solar cells. *Sol Energy Mater Sol Cells*. 2018;181:9-14.
41. Stuckelberger J, Loper P, Ballif C, et al. Recombination analysis of phosphorus-doped nanostructured silicon oxide passivating electron contacts for silicon solar cells. *IEEE J Photovoltaics*. 2018;8(2):389-396.
42. Yang G, Ingenito A, Van Hameren N, Isabella O, Zeman M. Design and application of ion-implanted poly-Si passivating contacts for interdigitated back contact c-Si solar cells. *Appl Phys Lett*. 2016;108(3):033903.
43. Kang J, Liu W, Allen T, de Bastiani, Yang X, de Wolf. Intrinsic silicon buffer layer improves hole-collecting poly-Si passivating contact. *Adv Mater Interfaces*. 2020;7(13):2000188.
44. Stodolny IGRMK, Anker J, Tool CJJ, et al. Novel schemes of p+ polySi hydrogenation implemented in industrial 6" bifacial front-and-rear passivating contacts solar cells. Proc. the35th Eur. Photovolt. Sol. Energy Conf. Exhib., pp. 3-6; 2018.
45. Nogay G, Stuckelberger J, Wyss P, et al. Silicon-rich silicon carbide hole-selective rear contacts for crystalline-silicon-based solar cells. *ACS Appl Mater Interfaces*. 2016;8(51):35660-35667.
46. Sinton RA, Cuevas A. Contactless determination of current-voltage characteristics and minority-carrier lifetimes in semiconductors from quasi-steady-state photoconductance data. *Appl Phys Lett*. 1996;69(17):2510-2512.
47. Santbergen R, Yang G, Procel P, et al. Optical analysis of poly-Si and poly-SiOx carrier-selective passivating contacts for c-Si solar cells. Light. Energy Environ. OSA Tech. Dig., p. PW3A.5; 2017.
48. Kruzelecky RV, Ukah C, Racansky D, Zukotynski S, Perz JM. Interband optical absorption in amorphous silicon. *J Non Cryst Solids*. 1988;103(2):234-249.
49. Holman ZC, Descoeudres A, Barraud L, et al. Current losses at the front of silicon heterojunction solar cells. *IEEE J Photovoltaics*. 2012;2(1):7-15.
50. Yang G. High-efficient n-i-p thin-film silicon solar cells. 2015.
51. Zhao Y, Mazzarella L, Procel P, et al. Doped hydrogenated nanocrystalline silicon oxide layers for high-efficiency c-Si heterojunction solar cells. *Prog Photovolt Res Appl*. 2020;28:425-435.
52. Li S, Pomaska M, Hoß J, et al. High-quality amorphous silicon thin films for tunnel oxide passivating contacts deposited at over 150 nm/-min. *Prog Photovolt Res Appl*. 2021;29:16-23.
53. Feldmann F, Schön J, Niess J, Lerch W, Hermle M. Studying dopant diffusion from poly-Si passivating contacts. *Sol Energy Mater Sol Cells*. 2019;200:109978.
54. Guthrey H, Lima Salles C, Kale AS, et al. Effect of surface texture on pinhole formation in SiOx-based passivated contacts for high-performance silicon solar cells. *ACS Appl Mater Interfaces*. 2020;12(50):55737-55745.
55. Yang G, Guo P, Procel P, et al. High-efficiency black IBC c-Si solar cells with poly-Si as carrier-selective passivating contacts. *Sol Energy Mater Sol Cells*. 2018;186:9-13.
56. Han C, Yang G, Montes A, et al. Realizing the potential of RF-sputtered hydrogenated fluorine-doped indium oxide as an electrode material for ultrathin SiO x/poly-Si passivating contacts. *ACS Appl Energy Mater*. 2020;3(9):8606-8618.
57. Zhang S, Pan X, Jiao H, et al. 335-W world-record p-type monocrystalline module with 20.6% efficient PERC solar cells. *IEEE J Photovoltaics*. 2015;6(1):145-152.
58. Ru X, Qu M, Wang J, et al. 25.11% efficiency silicon heterojunction solar cell with low deposition rate intrinsic amorphous silicon buffer layers. *Sol Energy Mater Sol Cells*. 2020;215:110643.

How to cite this article: Yang G, Han C, Procel P, et al. Oxygen-alloyed poly-Si passivating contacts for high-thermal budget c-Si heterojunction solar cells. *Prog Photovolt Res Appl*. 2022;30(2):141-151. doi:10.1002/pip.3472